Experimental Study of MIMO Channel Statistics and Capacity via Virtual Channel Representation

Yan Zhou[1], *Markus Herdin*[2], *Akbar M. Sayeed*[1], *Ernst Bonek*[2]

[1] Department of ECE, University of Wisconsin–Madison, Madison, WI 53706, USA
[2] Institute of Communications and Radio Frequency Engineering, Vienna University of Technology, Vienna A-1040, Austria

Corresponding author:
Akbar M. Sayeed
Department of Electrical and Computer Engineering
University of Wisconsin–Madison
1415 Engineering Drive
Madison,WI 53706
Email: akbar@engr.wisc.edu
Phone: (608)265-4731, Fax: (608)265-4623

Abstract

This work presents an experimental study of MIMO channel statistics and capacity via the recently proposed virtual channel representation, which describes the channel by a finite number of fixed virtual transmit/receive angles and delays. Our results confirm two important implications of virtual path partitioning: the virtual coefficients are approximately uncorrelated, and there exist fundamental angle-delay dependencies which limit the degrees of freedom in MIMO channels. The virtual channel power matrix reflects the distribution of channel power in angle-delay domain, quantifies the spatial-frequency correlation of actual channel coefficients, and also provides an intuitive explanation of the impact of scattering environments on capacity. The modeling accuracy of the popular Kronecker model, as well as the recently proposed eigenbeam model, is compared to the virtual channel model. The results indicate that both the virtual and eigenbeam models achieve good prediction accuracy, because they can model non-separable 2D angular spectrum, while the Kronecker model results in larger prediction error due to the restrictive structure.

1 Introduction

Recent research results have revealed tremendous capacity improvement achieved by Multiple-Input-Multiple-Output (MIMO) systems [1][2] which employ antenna arrays at both sides to create multiple parallel channels between transmitter and receiver and increase data rates without additional power or bandwidth consumption. While initial studies were based on an idealized i.i.d. channel model, recent analytical and experimental results show that the statistics of MIMO channels, especially the correlation between antennas, have a significant impact on channel capacity [3][5][11][17]. Moreover, MIMO systems are expected to support high-data-rate communications, which inherently requires large bandwidths and inevitably leads to frequency-selective channels. Therefore, a better understanding of wideband MIMO channels is critical for the design and performance prediction of MIMO systems.

Many channel models have been proposed to study the MIMO system performance and can be basically classified as propagation-inspired and analytic models. Propagation-inspired models [8]–[10] are aimed at describing the channel via individual physical paths. Each path is associated with distinct transmit/receive angles, delay, doppler shift, and complex path amplitude. Although it is quite accurate, the large number of non-linear physical parameters make propagation-inspired models difficult for theoretic analysis. Instead of modeling each individual path, analytical models are aimed at modeling the joint statistics of channel coefficients. Initial studies assumed that the channel coefficients associated with different transmit/receive antenna pairs are uncorrelated Gaussian random variables. This assumption corresponds to a rich scattering environment and promises a linear capacity growth with the minimum of the number of transmit and receive antennas [1][2]. However, recent experimental and analytical investigations have revealed that the realistic MIMO channels show significantly lower capacity due to the correlation of channel coefficients [3][6][7][11]. To incorporate correlation, the Kronecker model [4][3][22] has been proposed and assumes that the channel correlation is a product of the correlations at the transmitter and receiver sides. Based on this assumption, it models the channel matrix as a product of receive and transmit correlation matrices and an i.i.d. Gaussian random matrix. The product correlation assumption implies a product structure on the 2D angular power spectrum, which is usually not the case in realistic channel as exposed by recent experimental results [17][18] as well as the results reported in this paper.

The recently proposed virtual channel representation for Uniform Linear Arrays (ULA) [11] [12] [14] provides an intuitive and tractable representation of MIMO channel and yields

many insights into channel statistics and capacity behavior. Virtual representation is essentially a 2D Fourier transform of the actual channel matrix, and the transformed matrix can be modeled as an elementwise product of a virtual channel power matrix and an i.i.d. Gaussian random matrix. Therefore, unlike the Kronecker model, the non-separable channel statistics are preserved. Virtual channel representation can be easily extended to the time-varying frequency-selective scenario [12]. Through a 4D Fourier transform, it characterizes the channel by finite number of uniformly spaced and fixed virtual transmit/receive angles, virtual delays, and virtual Doppler shifts. Those virtual channel coefficients are uniform samples of a smoothed version of the 4D physical angle-delay-Doppler spectrum at a resolution determined by array aperture, bandwidth, and signaling duration. Instead of being characterized by each individual path, the actual channel matrix is efficiently represented by the simple 4D virtual channel power matrix with finite dimensions, which greatly simplifies the analysis and sheds light on channel statistics and capacity behavior. To date, virtual representation model has been successively applied to capacity scaling analysis [14], channel estimation [20], and space-time code design [19][21].

Motivated by both the virtual and Kronecker models, the eigenbeam model has been recently reported in [23][26][24]. Instead of using Fourier basis, it employs eigenbasis of transmit and receive correlation matrices as in Kronecker model to decompose the actual channel matrix and hence is applicable to arbitrary array geometries. Similar to the virtual model, the decomposed channel matrix is modeled as an elementwise product of an eigen-coupling matrix and an i.i.d. Gaussian random matrix. Therefore, both virtual and eigenbeam models preserve the non-separable channel statistics. In fact, the eigenbeam model is a generalization of the virtual model to non-ULA's for large number of antennas, since the Fourier basis vectors in the virtual representation are the exact eigenfunctions of the MIMO channel matrix for ULA's in the limit of large number of antennas.

The contributions of this paper lie in two aspects. (1) The statistics of both the virtual and actual channel coefficients have been experimentally investigated and interpreted via the concept of virtual path partitioning. Their potential applications to wireless communications have also been identified. (2) The impact of scattering environments on capacity has been explored both analytically and experimentally. The virtual channel model is also compared to other channel models in terms of capacity prediction accuracy.

The paper is organized as follows. In Section II, we introduce wideband and narrowband virtual channel representations as well as the definitions of virtual path partitioning and virtual channel power matrix. In Section III, we present a capacity analysis based on virtual representation and review several popular channel models for capacity prediction. In Section IV, the measurement results are discussed based on the theory in Section II and III. Section V contains concluding remarks.

2 Virtual Channel Representation

Consider a MIMO system with Uniform Linear Arrays (ULA) at both ends with N_T transmit antennas and N_R receive antennas. The array steering and response vectors are given by

$$\boldsymbol{a}_T(\theta_T) = \left[1, e^{-j2\pi\theta_T}, \ldots, e^{-j2\pi(N_T-1)\theta_T}\right]^T, \quad \boldsymbol{a}_R(\theta_R) = \left[1, e^{-j2\pi\theta_R}, \ldots, e^{-j2\pi(N_R-1)\theta_R}\right]^T. \tag{1}$$

The parameter θ is related to the physical angle[1] ϕ as $\theta = d\sin\phi/\lambda = \alpha\sin\phi$, where λ is the wavelength of propagation, d is the antenna spacing, and $\alpha = d/\lambda$ is the normalized antenna

[1] measured w.r.t. the array broadside

spacing. In case of $\alpha = 0.5$, there is a one-to-one mapping between $\theta \in [-0.5, 0.5]$ and $\phi \in [-\pi/2, \pi/2]$. For a slowly time-varying channel, the $N_R \times N_T$ frequency response channel matrix is

$$\mathbf{H}_c(f) = \sum_{n=1}^{N_{\text{path}}} \beta_n \boldsymbol{a}_R(\theta_{R,n}) \boldsymbol{a}_T^H(\theta_{T,n}) e^{-j2\pi\tau_n f}, \qquad -W/2 \le f \le W/2 \tag{2}$$

where W represents the two-sided bandwidth, and N_{path} is the number of paths. For the n-th path, $\beta_n = \alpha_n e^{j\phi_n}$ denotes the complex path amplitude with envelope $\alpha_n > 0$ and phase $\phi_n \in [0, 2\pi]$, the path delay τ_n is within the delay spread $[0, \tau_{DS}]$, and the receive and transmit path angles $\theta_{R,n}$ and $\theta_{T,n}$ are within the angular spreads $[\theta_{R-}, \theta_{R+}]$ and $[\theta_{T-}, \theta_{T+}]$, respectively. For a given scattering environment, $\{\alpha_n\}$, $\{\tau_n\}$, $\{\theta_{R,n}\}$, and $\{\theta_{T,n}\}$ are fixed, while $\{\phi_n\}$ randomly change for different channel realizations. In addition. the entries of $\mathbf{H}_c(f)$ can be specified as

$$H_c(i,k,f) = \sum_{n=1}^{N_{\text{paths}}} \beta_n e^{-j2\pi(i-1)\theta_{R,n}} e^{j2\pi(k-1)\theta_{T,n}} e^{-j2\pi\tau_n f}. \tag{3}$$

In (2), the physical paths are associated with the arbitrary receive/transmit angles and delays distributed within the angular and delay spreads. Instead of the physical paths, the virtual channel representation describes the channel via the virtual paths at the fixed and uniformly spaced virtual receive/transmit angles and delays, which are defined as

$$\widetilde{\theta}_{R,q} = \frac{q - \widetilde{N}_R}{N_R},\ q = 1, \ldots, N_R, \qquad \widetilde{\theta}_{T,p} = \frac{p - \widetilde{N}_T}{N_T},\ p = 1, \ldots, N_T, \qquad l/W,\ l = 0, \ldots, L \tag{4}$$

where $\widetilde{N}_R = (N_R+1)/2$, $\widetilde{N}_T = (N_T+1)/2$, and $L = \lceil W\tau_{DS} \rceil$. The spacings between the virtual angles and the virtual delays are determined by the array apertures ($\Delta\theta_R = 1/N_R, \Delta\theta_T = 1/N_T$) and the bandwidth ($\Delta\tau = 1/W$), respectively. The partial virtual channel representation w.r.t. space is given by the spatial Fourier transform of $\mathbf{H}_c(f)$

$$\mathbf{H}(f) = \mathbf{A}_R^H \mathbf{H}_c(f) \mathbf{A}_T, \quad \mathbf{H}_c(f) = \mathbf{A}_R \mathbf{H}(f) \mathbf{A}_T^H \tag{5}$$

where $\mathbf{A}_R = \big[\boldsymbol{a}_R(\widetilde{\theta}_{R,1}), \ldots, \boldsymbol{a}_R(\widetilde{\theta}_{R,N_R})\big]/\sqrt{N_R}$ and $\mathbf{A}_T = \big[\boldsymbol{a}_T(\widetilde{\theta}_{T,1}), \ldots, \boldsymbol{a}_T(\widetilde{\theta}_{T,N_T})\big]/\sqrt{N_T}$ are unitary Discrete Fourier Transform (DFT) matrices, which transform the channel matrix from the spatial domain to the virtual angle domain. The wideband virtual channel representation w.r.t. frequency is defined as the element-wise Fourier series expansion of $\mathbf{H}(f)$ [12]

$$\mathbf{H}(l) = \frac{1}{W} \int_{-W/2}^{W/2} \mathbf{H}(f) e^{j2\pi \frac{l}{W} f} df, \quad \mathbf{H}(f) = \sum_{l=0}^{L} \mathbf{H}(l) e^{-j2\pi \frac{l}{W} f} \tag{6}$$

which means that the channel frequency response is represented via the discrete virtual delays. The wideband virtual channel coefficients in $\mathbf{H}(l)$ can be specified as

$$\begin{aligned} H(q,p,l) &= \sum_{n=1}^{N_{\text{path}}} \beta_n \frac{\big[\boldsymbol{a}_R^H(\widetilde{\theta}_{R,q}) \boldsymbol{a}_R(\theta_{R,n})\big]}{\sqrt{N_R}} \frac{\big[\boldsymbol{a}_T^H(\theta_{T,n}) \boldsymbol{a}_T(\widetilde{\theta}_{T,p})\big]}{\sqrt{N_T}} \frac{1}{W} \int_{-W/2}^{W/2} e^{j2\pi(l/W - \tau_n)f} df \\ &\triangleq \sum_{n=1}^{N_{\text{path}}} \beta_n f_{N_R}(\theta_{R,n} - \widetilde{\theta}_{R,q}) f_{N_T}^*(\theta_{T,n} - \widetilde{\theta}_{T,p}) \text{sinc}(W\tau_n - l) \end{aligned} \tag{7}$$

$$f_N(\theta) = \frac{1}{\sqrt{N}} \sum_{i=0}^{N-1} e^{-j2\pi\theta i} = \frac{1}{\sqrt{N}} e^{-j\pi\theta(N-1)} \frac{\sin(\pi N\theta)}{\sin(\pi\theta)}, \quad \text{sinc}(x) = \frac{\sin(\pi x)}{\pi x}.$$

The physical meaning of $H(q,p,l)$ is well exposed by the relation between $\mathbf{H}_c(f)$ and $\mathbf{H}(l)$

$$\mathbf{H}_c(f) = \sum_{l=0}^{L} \mathbf{A}_R \mathbf{H}(l) \mathbf{A}_T^H \, e^{-j2\pi \frac{l}{W} f} = \sum_{l=0}^{L} \sum_{q=1}^{N_R} \sum_{p=1}^{N_T} H(q,p,l) \boldsymbol{a}_R(\widetilde{\theta}_{R,q}) \boldsymbol{a}_T^H(\widetilde{\theta}_{T,p}) \, e^{-j2\pi \frac{l}{W} f} \quad (8)$$

which is derived by combining (5) and (6) and indicates that $H(q,p,l)$ is the amplitude of a virtual path at the fixed angles $\widetilde{\theta}_{R,q}$ and $\widetilde{\theta}_{T,p}$ and the fixed delay l/W. Furthermore, the entries of $\mathbf{H}_c(f)$ are related to $\{H(q,p,l)\}$ via the 3D DFT

$$H_c(i,k,f) = \frac{1}{\sqrt{N_R N_T}} \sum_{l=0}^{L} \sum_{q=1}^{N_R} \sum_{p=1}^{N_T} H(q,p,l) \, e^{-j2\pi(i-1)\widetilde{\theta}_{R,q}} \, e^{j2\pi(k-1)\widetilde{\theta}_{T,p}} \, e^{-j2\pi \frac{l}{W} f}. \quad (9)$$

The reason why express the channel matrix via the virtual channel coefficients $\{H(q,p,l)\}$ instead of the actual channel coefficients $\{H_c(i,k,f)\}$ or the physical path parameters is because the non-vanishing $H(q,p,l)$'s capture the essential degrees of freedom in the channel and hence represent the channel with the minimum number of parameters, which greatly simplifies the channel estimation and feedback as demonstrated in the experimental results.

When W is much smaller than the channel coherence bandwidth $1/\tau_{DS}$, $\mathbf{H}_c(f)$ is approximately the same as $\mathbf{H}_c(0)$, which gives the narrowband spatial-domain channel matrix

$$\mathbf{H}_c = \mathbf{H}_c(0) = \sum_{n=1}^{N_{\text{path}}} \beta_n \boldsymbol{a}_R(\theta_{R,n}) \boldsymbol{a}_T^H(\theta_{T,n}). \quad (10)$$

The narrowband virtual channel representation is defined as the spatial Fourier transform of $\mathbf{H}_c$ [11]

$$\mathbf{H} = \mathbf{A}_R^H \mathbf{H}_c \mathbf{A}_T, \quad \mathbf{H}_c = \mathbf{A}_R \mathbf{H} \mathbf{A}_T^H = \sum_{q=1}^{N_R} \sum_{p=1}^{N_T} H(q,p) \boldsymbol{a}_R(\widetilde{\theta}_{R,q}) \boldsymbol{a}_T^H(\widetilde{\theta}_{T,p}). \quad (11)$$

The narrowband virtual channel coefficients in $\mathbf{H}$ can be specified as

$$H(q,p) = \sum_{n=1}^{N_{\text{path}}} \beta_n f_{N_R}(\theta_{R,n} - \widetilde{\theta}_{R,q}) f_{N_T}^*(\theta_{T,n} - \widetilde{\theta}_{T,p}) \quad (12)$$

where $f(\cdot)$ is defined in (7). The expansion of $\mathbf{H}_c$ in (11) indicates that $H(q,p)$ is the amplitude of a narrowband virtual path at the angles $\widetilde{\theta}_{R,q}$ and $\widetilde{\theta}_{T,p}$, and the entries of $\mathbf{H}_c$ are related to $\{H(q,p)\}$ via

$$H_c(i,k) = \frac{1}{\sqrt{N_R N_T}} \sum_{q=1}^{N_R} \sum_{p=1}^{N_T} H(q,p) e^{-j2\pi(i-1)\widetilde{\theta}_{R,q}} e^{j2\pi(k-1)\widetilde{\theta}_{T,p}}. \quad (13)$$

Furthermore, setting $f=0$ in (6) reveals that each narrowband virtual channel coefficient is the sum of the corresponding wideband virtual channel coefficients at different l's

$$\mathbf{H} = \mathbf{H}\,(f=0) = \sum_{l=0}^{L} \mathbf{H}(l), \quad H(q,p) = \sum_{l=0}^{L} H(q,p,l). \quad (14)$$

2.1 Virtual Path Partitioning

Virtual path partitioning reveals the approximately uncorrelated nature of the virtual channel coefficients. The wideband virtual representation introduces the following sets of physical paths

$$\begin{aligned} S_{R,q} &= \{n : -1/(2N_R) \le (\theta_{R,n} - \widetilde{\theta}_{R,q}) < 1/(2N_R)\} \\ S_{T,p} &= \{n : -1/(2N_T) \le (\theta_{T,n} - \widetilde{\theta}_{T,p}) < 1/(2N_T)\} \\ S_{\tau,l} &= \{n : -1/(2W) \le (\tau_n - l/W) < 1/(2W)\}. \end{aligned} \tag{15}$$

The above sets form a partition of the physical paths

$$\bigcup_{q,p,l} \left[S_{R,q} \cap S_{T,p} \cap S_{\tau,l}\right] \triangleq \bigcup_{q,p,l} S_{q,p,l} = \left\{1, \cdots, N_{\text{path}}\right\}. \tag{16}$$

The above path partitioning is illustrated in Fig.1, where the receive angle domain, transmit angle domain, and delay domain are divided into N_R, N_T, and L intervals with centers at $\{\widetilde{\theta}_{R,q}\}$, $\{\widetilde{\theta}_{T,p}\}$, and $\{l/W\}$, respectively. Those intervals partition the 3D angle-delay space into $N_R N_T L$ cuboids with equal size of $\frac{1}{N_R} \times \frac{1}{N_T} \times \frac{1}{W}$, and the $S_{q,p,l}$ in (16) represents the set of paths in the cuboid centered at $\left(\widetilde{\theta}_{R,q}, \widetilde{\theta}_{T,p}, l/W\right)$. With the virtual path partitioning, the wideband virtual channel coefficient in (7) can be approximated as

$$\begin{aligned} H(q,p,l) &\approx \sum_{n=1}^{N_{\text{path}}} \beta_n \left[f_{N_R}(0)\, 1_{\left(n \in S_{R,q}\right)}\right] \left[f^*_{N_T}(0)\, 1_{\left(n \in S_{T,p}\right)}\right] \left[\text{sinc}(0)\, 1_{\left(n \in S_{\tau,l}\right)}\right] \\ &= \sum_{n \in S_{q,p,l}} \beta_n f_{N_R}(0) f^*_{N_T}(0) \text{sinc}(0) = \sum_{n \in S_{q,p,l}} \beta_n \sqrt{N_R N_T} \end{aligned} \tag{17}$$

where $1_{(\cdot)}$ denotes the binary indicator function. The above approximation is due to the peakiness of $f_N(\theta)$ and $\text{sinc}(W\tau)$ around the origin and reveals the approximately uncorrelated nature of $\{H(q,p,l)\}$ [11, 12], since each $H(q,p,l)$ is contributed by the paths in a distinct set $S_{q,p,l}$.

In the narrowband case, the physical paths are not resolvable in the delay domain and hence are only partitioned in the angular domain

$$\bigcup_{q,p} \left[S_{R,q} \cap S_{T,p}\right] \triangleq \bigcup_{q,p} S_{q,p} = \left\{1, \cdots, N_{\text{path}}\right\}, \qquad S_{q,p} = \bigcup_{l} S_{q,p,l}. \tag{18}$$

The above partition means that the 2D angular domain is divided into $N_R N_T$ rectangles with equal size of $\frac{1}{N_R} \times \frac{1}{N_T}$, and $S_{q,p}$ represents the set of paths in the rectangle centered at $\left(\widetilde{\theta}_{R,q}, \widetilde{\theta}_{T,p}\right)$. Similarly, the narrowband virtual channel coefficient in (12) can be approximated as

$$H(q,p) \approx \sum_{n=1}^{N_{\text{path}}} \beta_n \left[f_{N_R}(0)\, 1_{\left(n \in S_{R,q}\right)}\right] \left[f^*_{N_T}(0)\, 1_{\left(n \in S_{T,p}\right)}\right] = \sum_{n \in S_{q,p}} \beta_n \sqrt{N_R N_T} \tag{19}$$

which implies that $\{H(q,p)\}$ are approximately uncorrelated, since each $H(q,p)$ is contributed by the paths in a distinct set $S_{q,p}$.

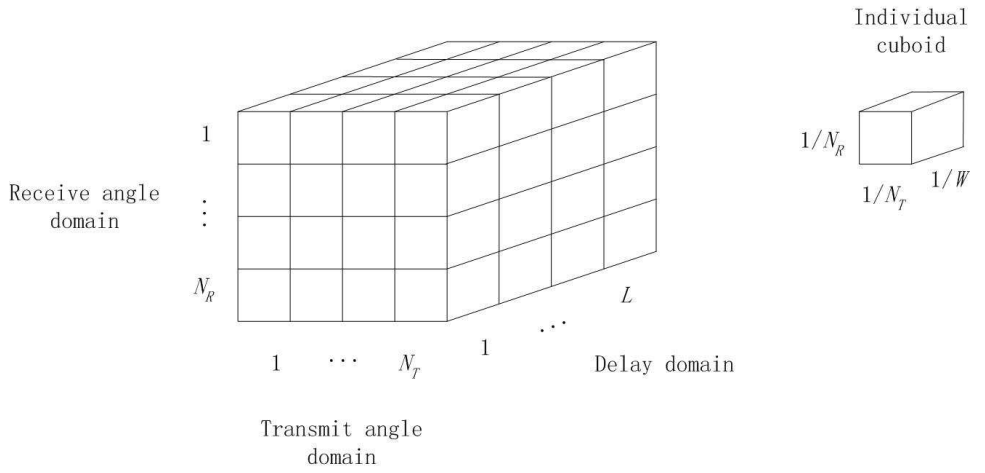

Figure 1: Illustration of wideband virtual path partitioning. The receive angle domain, transmit angle domain, and delay domain are divided into N_R, N_T, and L intervals, which partition the 3D angle-delay space into $N_R N_T L$ cuboids with equal size of $\frac{1}{N_R}\times\frac{1}{N_T}\times\frac{1}{W}$. The physical paths in the 3D space are partitioned into each individual cuboid.

2.2 Virtual Channel Power Matrix

The entries of the $N_R \times N_T$ wideband virtual channel power matrix $\mathbf{M}(l)$ are defined as

$$M(q,p,l) = E\left[|H(q,p,l)|^2\right] \approx \sum_{n\in S_{q,p,l}} \alpha_n^2 N_R N_T \tag{20}$$

which means that $M(q,p,l)$ is the power of the associated virtual path and is contributed by the total power of the physical paths in $S_{q,p,l}$. Intuitively, $\mathbf{M}(l)$ reflects the angular power distribution of the virtual paths at the l-th virtual delay. Due to the approximately uncorrelated nature of $\{H(q,p,l)\}$, the space-frequency correlation of the actual channel coefficients $\{H_c(i,k,f)\}$ specified in (3) and (9) is

$$E\big[H_c(i,k,f)H_c^*(i',k',f')\big] = \sum_{n=1}^{N_{\text{paths}}} \alpha_n^2 e^{-j2\pi(i-i')\theta_{R,n}} e^{j2\pi(k-k')\theta_{T,n}} e^{-j2\pi(f-f')\tau_n} \tag{21}$$

$$\approx \frac{1}{N_R N_T} \sum_{l=0}^{L} \sum_{q=1}^{N_R} \sum_{p=1}^{N_T} M(q,p,l)\; e^{-j2\pi(i-i')\widetilde{\theta}_{R,q}}\; e^{j2\pi(k-k')\widetilde{\theta}_{T,p}}\; e^{-j2\pi(f-f')l/W} \tag{22}$$

which implies that for ULA's, $\{H_c(i,k,f)\}$ form a 3D stationary process whose correlation is determined by $\{M(q,p,l)\}$, which serve as a 3D power spectrum in the virtual angle-delay domain.

Similarly, the entries of the $N_R \times N_T$ narrowband virtual channel power matrix $\mathbf{M}$ are defined as

$$M(q,p) = E\left[|H(q,p)|^2\right] \approx \sum_{n\in S_{q,p}} \alpha_n^2 N_R N_T \tag{23}$$

which indicates that $M(q,p)$ is the power of a narrowband virtual path at the angles $\widetilde{\theta}_{R,q}$ and $\widetilde{\theta}_{T,p}$ and, hence, $\mathbf{M}$ reflects the angular power distribution of the narrowband virtual paths. Since $\{H(q,p)\}$ are approximately uncorrelated, the spatial correlation of $\{H_c(i,k)\}$ in (13)

can be approximated as

$$E\big[H_c(i,k)H_c^*(i',k')\big] \approx \frac{1}{N_R N_T}\sum_{q=1}^{N_R}\sum_{p=1}^{N_T} M(q,p)\; e^{-j2\pi(i-i')\widetilde{\theta}_{R,q}}\; e^{j2\pi(k-k')\widetilde{\theta}_{T,p}} \tag{24}$$

which implies that $\{H_c(i,k)\}$ form a 2D stationary process whose correlation is determined by the 2D angular power spectrum $\{M(q,p)\}$.

3 Capacity Analysis and Prediction

3.1 Capacity of Different Scattering Environments

Due to the space limit, we only focus on the narrowband ergodic capacity [1]

$$C_{NB} = \max_{\mathrm{tr}(\mathbf{Q})\le\rho} E\big[\log_2\big|\mathbf{I}_{N_R} + \mathbf{H}_c\mathbf{Q}\mathbf{H}_c^H\big|\big] = \max_{\mathrm{tr}(\mathbf{\Lambda})\le\rho} E\big[\log_2\big|\mathbf{I}_{N_R} + \mathbf{H}\mathbf{\Lambda}\mathbf{H}^H\big|\big] \quad \text{bps/Hz} \tag{25}$$

where $\mathbf{Q}$ is the $N_T \times N_T$ input covariance matrix in the spatial domain, $\mathbf{\Lambda} = \mathbf{A}_T^H\mathbf{Q}\mathbf{A}_T$ is the input covariance matrix in the virtual angle domain, and the transmit SNR ρ is the ratio of the total transmit power to the noise power per receive antenna. The following analysis provides insights into the impact of scattering environments on C_{NB}. To investigate C_{NB}, we need to specify the optimum virtual input $\mathbf{\Lambda}_o$, which in general has to be numerically computed via optimization routines. However, by maximizing a capacity upper bound, we can get a closed-form suboptimum solution, which has similar behavior as $\mathbf{\Lambda}_o$. It has been shown in [13][26] that $\mathbf{\Lambda}_o$ is diagonal for uncorrelated virtual coefficients. Therefore, we choose $\mathbf{\Lambda} = \mathrm{diag}(\lambda_1,\ldots,\lambda_{N_T})$, and the term to be maximized in (25) can be upper bounded by

$$E\left[\log_2\big|\mathbf{I}_{N_R} + \mathbf{H}\mathbf{\Lambda}\mathbf{H}^H\big|\right] \le \log_2\big|\mathbf{I}_{N_T} + \mathbf{\Lambda}^{1/2}E\big[\mathbf{H}^H\mathbf{H}\big]\mathbf{\Lambda}^{1/2}\big| \le \sum_{p=1}^{N_T}\log_2\left(1+\lambda_p\sum_{q=1}^{N_R}M(q,p)\right)$$

where the first inequality results from the identity $|\mathbf{I}+\mathbf{A}\mathbf{B}| = |\mathbf{I}+\mathbf{B}\mathbf{A}|$ and the Jensen's inequality, and the Hadamard inequality is applied at the second step with $M(q,p)$ defined in (23). By maximizing the last term of the above expression, we get a suboptimum virtual input $\mathbf{\Lambda}_s$ whose diagonal entries are given by the standard waterfilling solution [25]

$$\lambda_{s,p} = \left(\mu - \frac{1}{\sum_{q=1}^{N_R} M(q,p)}\right)^+, \quad p = 1,\cdots,N_T \tag{26}$$

where $(x)^+ = \max(x,0)$ and μ is selected so that $\sum_{p=1}^{N_T}\lambda_{s,p} = \rho$. The above solution suggests that as $\rho \to 0$, all power will be allocated to the strongest transmit virtual angle whose index is denoted as p^*. Accordingly, $\mathbf{\Lambda}_s \overset{\rho\to 0}{\longrightarrow} \rho\mathbf{\Sigma}(p^*)$ where the $N_T \times N_T$ $\mathbf{\Sigma}(p^*)$ has one at the p^*-th diagonal entry and zero at other positions. However, as $\rho \to \infty$, (26) will equally allocate power to all non-vanishing transmit virtual angles. Therefore, $\mathbf{\Lambda}_s \overset{\rho\to\infty}{\longrightarrow} (\rho/N_T)\mathbf{I}_{N_T}$ if all transmit angles are non-vanishing, i.e. $\sum_{q=1}^{N_R}M(q,p) > 0$ for all p's, which is usually the case in the measurement. According to the experimental results, $\mathbf{\Lambda}_s$ almost achieves the same capacity as $\mathbf{\Lambda}_o$ under various measurement scenarios and SNRs. Therefore, one could interpret the behavior of C_{NB} via the expression of $\mathbf{\Lambda}_s$. After substituting $\mathbf{\Lambda}_s$ into (25) and using its asymptotical

results, we can show that at low and high SNRs, C_{NB} will be

$$\begin{aligned} C_{NB} &\overset{\rho\to 0}{\longrightarrow} C_0 = E\left[\log_2\left(1+\rho \parallel \boldsymbol{h}(p^*) \parallel_F^2\right)\right] \le \log_2\left(1+\rho\sum_{q=1}^{N_R} M(q,p^*)\right) \triangleq \bar{C}_0 \\ C_{NB} &\overset{\rho\to\infty}{\longrightarrow} C_\infty = E\left[\log_2\left|\mathbf{I}_{N_R}+\frac{\rho}{N_T}\mathbf{H}\mathbf{H}^H\right|\right] \le \min(B_T,B_R) \triangleq \bar{C}_\infty \end{aligned} \tag{27}$$

where $\boldsymbol{h}(p^*)$ denotes the p^*-th column of $\mathbf{H}$, and the Jensen's inequality is applied to get the upperbound of C_0. Both B_T and B_R are the upperbounds of C_∞ and are specified below

$$\begin{aligned} C_\infty &\le E\left[\sum_{q=1}^{N_R}\log_2\left(1+\frac{\rho}{N_T}\sum_{p=1}^{N_T}|H(q,p)|^2\right)\right] \le \sum_{q=1}^{N_R}\log_2\left(1+\frac{\rho}{N_T}\sum_{p=1}^{N_T}M(q,p)\right) \triangleq B_R \\ C_\infty &= E\left[\log_2\left|\mathbf{I}_{N_T}+\frac{\rho}{N_T}\mathbf{H}^H\mathbf{H}\right|\right] \le \sum_{p=1}^{N_T}\log_2\left(1+\frac{\rho}{N_T}\sum_{q=1}^{N_R}M(q,p)\right) \triangleq B_T \end{aligned} \tag{28}$$

where the Hadamard and Jensen's inequalities are applied sequentially to get the bounds.

As introduced earlier, $\mathbf{M}$ represents the 2D angular power spectrum, which is determined by the physical scattering environments. Suppose the total channel power $\sum_q\sum_p M(q,p)$ is fixed, the question is how will the distribution of $\{M(q,p)\}$ affect C_{NB}? The bounds in (27) provide insights into this problem. At the low SNR, it is easy to see that the optimum $\mathbf{M}$ maximizing $\bar{C}_0$ has all the non-vanishing entries distributed in the p^*-th column. This is because the water-filling power allocation only excites the strongest transmit virtual angle and, hence, the best channel would focus all the channel power on the corresponding column of $\mathbf{M}$. At the high SNR, B_R and B_T in (28) can be approximated as

$$B_R \approx \log_2\left(\left(\frac{\rho}{N_T}\right)^{N_R}\prod_{q=1}^{N_R}\left[\sum_{p=1}^{N_T}M(q,p)\right]\right),\ B_T \approx \log_2\left(\left(\frac{\rho}{N_T}\right)^{N_T}\prod_{p=1}^{N_T}\left[\sum_{q=1}^{N_R}M(q,p)\right]\right).$$

According to the inequality of arithmetic and geometric means, B_R and B_T are maximized when $\sum_{p=1}^{N_T}M(q,p)$ is the same for all q and $\sum_{q=1}^{N_R}M(q,p)$ is the same for all p. Therefore, the upper bound $\bar{C}_\infty$ will be maximized if both conditions are satisfied. The corresponding $\mathbf{M}$ can be an equal-value matrix or a diagonal matrix with equal value in the main diagonal. Intuitively, the best channel at the high SNR will make all the receive and transmit angles non-vanishing to maximize the multiplexing gain, which is reflected by the rank of $\mathbf{H}$.

3.2 Capacity Prediction by Different Channel Models

In this section, we review several popular narrowband channel models and describe the inherent relationship among them. Their capacity-prediction performance is compared in Section IV-F. The narrowband virtual channel model synthesizes the spatial-domain channel matrix $\mathbf{H}_c$ according to

$$\widehat{\mathbf{H}}_{\text{vir}} = \mathbf{A}_R(\sqrt{\mathbf{M}}\odot\mathbf{G})\mathbf{A}_T^H \tag{29}$$

where the $N_R\times N_T$ matrix $\mathbf{G}$ consists of i.i.d. complex Gaussian entries with zero mean and unit variance, while $\odot$ and $\sqrt{(\cdot)}$ represent the element-wise product and square root. By varying the values of the entries in $\mathbf{M}$, one can easily simulate different scattering environments. The Kronecker channel model [4][3][22] synthesizes $\mathbf{H}_c$ according to

$$\widehat{\mathbf{H}}_{\text{Kron}} = \mathbf{R}_R^{1/2}\mathbf{G}\mathbf{R}_T^{1/2} \tag{30}$$

where $\mathbf{R}_R = E[\mathbf{H}_c\mathbf{H}_c^H]$ and $\mathbf{R}_T = E[\mathbf{H}_c^H\mathbf{H}_c]$ represent the receive and transmit correlation matrices, respectively. The Kronecker model assumes that the spatial correlation is a product of the transmit and receive correlations and therefore imposes a product structure on the 2D angular spectrum, as elaborated in the measurement results. Motivated by both the virtual model and the Kronecker model, the recently proposed eigenbeam model [23][26] transforms $\mathbf{H}_c$ with the eigenbasis

$$\mathbf{H}_{\text{eig}} = \mathbf{U}_R^H\mathbf{H}_c\mathbf{U}_T \tag{31}$$

where $\mathbf{U}_R$ and $\mathbf{U}_T$ consist of the orthonormal eigenvectors of $\mathbf{R}_R$ and $\mathbf{R}_T$, respectively. Next, the eigenmode coupling matrix $\mathbf{\Omega}$ is formed with $\Omega(q,p) = E[|H_{\text{eig}}(q,p)|^2]$, and the synthesized $\mathbf{H}_c$ is

$$\widehat{\mathbf{H}}_{\text{eig}} = \mathbf{U}_R(\sqrt{\mathbf{\Omega}} \odot \mathbf{G})\mathbf{U}_T^H. \tag{32}$$

To reveal the inherent relationship among the three channel models, we rewrite (30) as

$$\widehat{\mathbf{H}}_{\text{Kron}} = \mathbf{U}_R\mathbf{D}_R^{1/2}\mathbf{U}_R^H\mathbf{G}\mathbf{U}_T\mathbf{D}_T^{1/2}\mathbf{U}_T^H \triangleq \mathbf{U}_R(\mathbf{D}_R^{1/2}\mathbf{G}'\mathbf{D}_T^{1/2})\mathbf{U}_T^H \tag{33}$$

where the diagonal matrices $\mathbf{D}_R$ and $\mathbf{D}_T$ contain the eigenvalues of $\mathbf{R}_R$ and $\mathbf{R}_T$, and $\mathbf{G}'$ is a unitary transform of the i.i.d. matrix $\mathbf{G}$ and hence is also an i.i.d. matrix. Comparing (29), (32), and (33), we observe that the Kronecker model essentially assumes separable[2] spectrum, while both the virtual and eigenbeam models assume non-separable spectrum. On the other hand, the virtual model is only applicable to ULA's, while both the Kronecker and eigenbeam models are also applicable to non-ULA's due to the use of transmit and receive eigenbasis. In fact, the eigenbeam model is motivated by both the virtual and Kronecker models and can be regarded as a generalization of the virtual model to non-ULA's in the limit of large number of antennas, since the eigenbasis will converge to the Fourier basis.

4 Measurement Results

4.1 Measurement Setup and Channel Normalization

The measurement was conducted at the third floor of the Institute of Communications and Radio Frequency Engineering at Vienna University of Technology, Austria. Fig.2 shows the partial floor plan. The transmitter was fixed in the corridor. A monopole antenna was mounted on a 2D positioning table and was moved to 20 x-coordinates and 10 y-coordinates on a rectangular grid with $\lambda/2$ spacing. The receiver employs a $\lambda/2$ spaced 8-element ULA and was placed at different positions with 3 different broadside directions D1-D3. Each combination of receiver position and direction corresponds to a measurement scenario. The total measurement bandwidth was $W = 120$MHz at a center frequency of 5.2GHz. Within the bandwidth, the MIMO channel matrix is measured at $N_F = 193$ equidistant frequencies with spacing $\Delta f = 0.62$MHz. For each scenario at a particular frequency f, the receive ULA recorded the channel vector for each of 200 transmitter monopole positions. 8 adjacent transmitter positions in the x direction were further selected to form a 8-element virtual TX array and, hence, the 200 measured channel vectors provide 130 8×8 $\mathbf{H}_c(f)$ realizations. Detailed measurement setup is reported in [16][17].

In the wideband case, each measured $\mathbf{H}_c(f)$ realization is approximated by a piece-wise constant function: $\mathbf{H}_c(f) = \sum_{m=1}^{N_F} \mathbf{H}_c(f_m) I_{[f_m - \Delta f/2, f_m + \Delta f/2)}$, where $I_{[a,b)}$ is the function with 1 in $[a,b)$ and 0 elsewhere, $f_m = (m - (N_F+1)/2)\,\Delta f$ denotes the m-th frequency, and

[2]which means that the variance of each entry in $\mathbf{D}_R^{1/2}\mathbf{G}'\mathbf{D}_T^{1/2}$ has a product form.

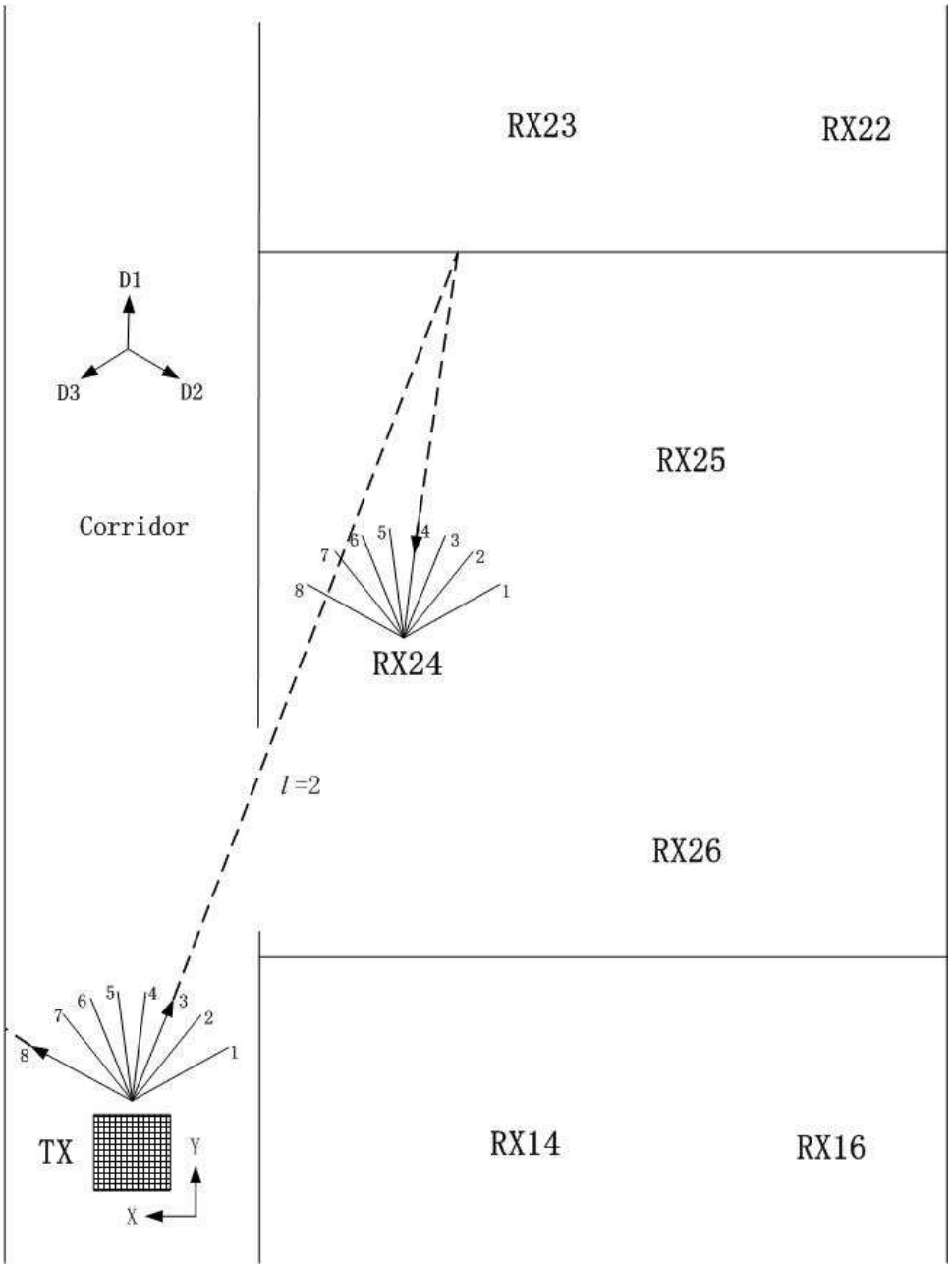

Figure 2: Floor plan of the corridor and office rooms.

$N_F \Delta f = W$. The $\mathbf{H}_c(f)$ realizations are further normalized according to $\frac{1}{W} \int_{-W/2}^{W/2} E\Big\{ \mathrm{tr}\big[\mathbf{H}_c(f) \mathbf{H}_c^H(f)\big] \Big\} df = N_R N_T$, where $N_R = N_T = 8$ for this measurement. In the narrowband case, the $\mathbf{H}_c$ realizations measured at the central frequency are normalized based on $E\Big\{ \mathrm{tr}\big[\mathbf{H}_c \mathbf{H}_c^H\big] \Big\} = N_R N_T$, which is also applied to the channel realizations synthesized by the channel models in Section III-B.

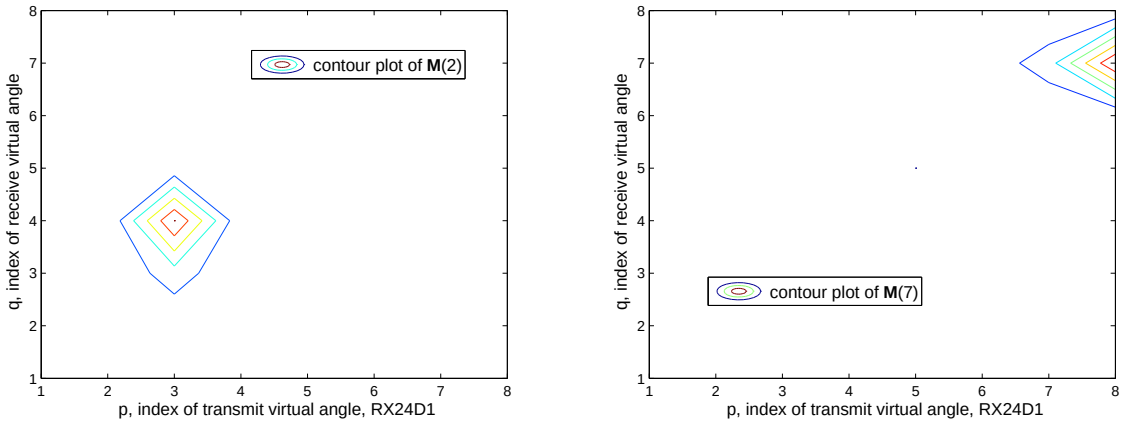

Figure 3: Contour plot of wideband virtual channel power matrix $\mathbf{M}(l)$. (a) $l = 2$. (b) $l = 7$.

4.2 Angle-Delay Dependencies

In the wideband situation, (8) indicates that the channel can be represented by the virtual paths at the fixed virtual angles and delays with the amplitudes $\{H(q,p,l)\}$ and the powers $\{M(q,p,l)\}$. In fact, the wideband virtual channel power matrix $\mathbf{M}(l)$ in (20) represents the angular power spectrum conditioned on the l-th virtual delay, and the dominant $M(q,p,l)$'s expose the positions of the dominant virtual paths. For instance, the contour plot of the $\mathbf{M}(2)$ measured at RX24D1 is shown in Fig.3 (a), where the dominant entry $M(4,3,2)$ represents a dominant virtual path propagating from the 3rd transmit virtual angle to the 4th receive virtual angle at the 2nd virtual delay. The propagation geometry is also depicted in Fig.2, where the eight physical angles corresponding to their virtual counterparts are marked at both sides. In the narrowband situation, (11) implies that the channel can be represented by the narrowband virtual paths at the fixed virtual angles with the amplitudes $\{H(q,p)\}$ and the powers $\{M(q,p)\}$. It can be shown via (14) that the narrowband virtual channel power matrix $\mathbf{M}$ in (23) is the sum of $\mathbf{M}(l)$ at different l's, since the narrowband virtual paths are not resolvable in the delay domain. The measured $\mathbf{M}$ at RX24D1 is illustrated in Fig.4, where the 4 dominant entries represent the 4 dominant narrowband virtual paths at the 4 distinct angular positions.

One important observation revealed by the experimental results is the angle-delay dependencies, which state that the conditional angular spectrum $\mathbf{M}(l)$ varies with the virtual delay index l. This can be seen from Fig.3, where the measured $\mathbf{M}(2)$ and $\mathbf{M}(7)$ at RX24D1 exhibit different patterns. Moreover, by comparing Fig.3 with Fig.4, one can observe that the dominant entries in each $\mathbf{M}(l)$ have a smaller angular spread than those in the narrowband angular spectrum $\mathbf{M}$. This implies that the dominant entries in $\{\mathbf{M}(l), l = 0,\ldots,L\}$ have a sparser distribution than those in $\mathbf{M}$.

An application of the sparse distribution is the low-rank approximation of the channel matrix. The measured channel matrices in the space-frequency domain are denoted as $\{\mathbf{H}_c(f_m)\}_{m=1}^{N_F}$, which can be represented by the $N_R N_T N_F = 8{\times}8{\times}193 = 12352$ space-frequency channel coefficients or by the physical path parameters whose number is in the order of N_{path}, as shown in (2). In the virtual domain, the experimental results indicate that 95% of the total channel power[3] is contributed by the powers of 331 $H(q,p,l)$'s. It means that the channel can be efficiently represented by the 331 virtual channel coefficients via (8) instead of the 12352 actual channel

[3]The sum of all $M(q,p,l)$'s.

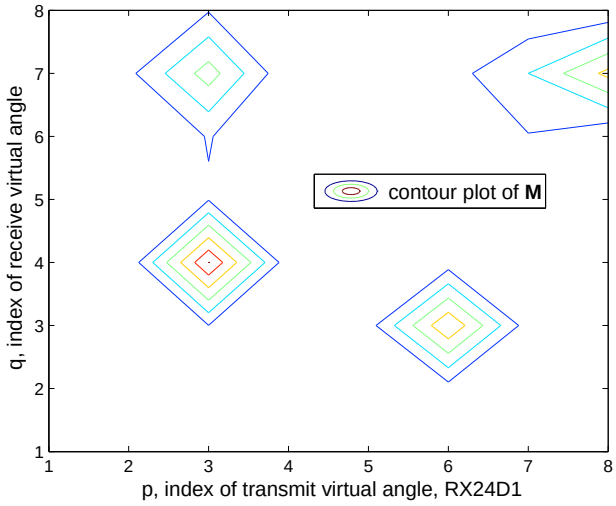

Figure 4: Contour plot of narrowband virtual channel power matrix $\mathbf{M}$.

coefficients or the large number[4] of physical path parameters. The low-rank approximation can simplify the channel feedback in wireless communications. Meanwhile, it also simplifies the channel estimation, since $\{H(q,p,l)\}$ can be easily obtained from $\{\mathbf{H}_c(f_m)\}$ via the Fourier transform, while the estimation of physical path parameters is in general challenging in practice, especially when N_{path} is large.

4.3 Statistics of Virtual Channel Coefficients

The correlation matrix for the wideband virtual channel coefficients is defined as $\mathbf{R}=E[\boldsymbol{h}\boldsymbol{h}^H]$ with the vector $\boldsymbol{h}$ comprising the $N_R N_T L$ elements in $\{H(q,p,l)\}$. The experimental results show that $\mathbf{R}$ is approximately diagonal. Specifically, let $\mathbf{R}_{\text{diag}}$ be the diagonal matrix containing the diagonal entries of $\mathbf{R}$. The normalized mean square error $\|\mathbf{R}-\mathbf{R}_{\text{diag}}\|_F^2 / \|\mathbf{R}\|_F^2$ measured at different sites is found to be between 0.018 and 0.031, which shows a good match of them. The approximate diagonal structure implies that $\{H(q,p,l)\}$ are approximately uncorrelated. This can be understood via the virtual path partitioning in (17), which indicates that each $H(q,p,l)$ is contributed by the paths in a distinct set $S_{q,p,l}$. Similarly, the correlation matrix for the narrowband virtual channel coefficients is defined as $\bar{\mathbf{R}}=E[\bar{\boldsymbol{h}}\bar{\boldsymbol{h}}^H]$ with $\bar{\boldsymbol{h}}$ comprising the $N_R N_T$ elements in $\{H(q,p)\}$. The experimental results show that $\bar{\mathbf{R}}$ is also approximately diagonal with the measured $\|\bar{\mathbf{R}}-\bar{\mathbf{R}}_{\text{diag}}\|_F^2 / \|\bar{\mathbf{R}}\|_F^2$ varying from 0.02 to 0.037. The contour plot of the $\bar{\mathbf{R}}$ measured at RX24D1 is illustrated in Fig.5, where the 4 dominant diagonal entries represent the powers of the 4 dominant narrowband virtual paths.

We next investigate the marginal statistics of individual virtual channel coefficients. The experimental results show that the virtual channel coefficients have zero mean but may not have Gaussian distribution. The Cumulative Distribution Function (CDF) for the real part of $H(7,8,7)$ measured at Rx24D1 is plotted in Fig.6, where the CDF obviously deviates from the Gaussian distribution. It can be seen from (17) that $H(q,p,l)$ is contributed by the physical paths in $S_{q,p,l}$, whose number may not be large enough to make the distribution close to be[5] Gaussian. In fact, the distribution of $H(7,8,7)$ matches that of the sum of two physical paths $X=Ce^{j\phi_1}+0.2Ce^{j\phi_2}$, where ϕ_l is the random path phase and the constant path amplitude C

[4] which should be greater than 331, since each non-vanishing $H(q,p,l)$ is contributed by physical paths in $S_{q,p,l}$ in (17).

[5] According to the central limit theorem, the Gaussian distribution would be accurate if the number of paths is large.

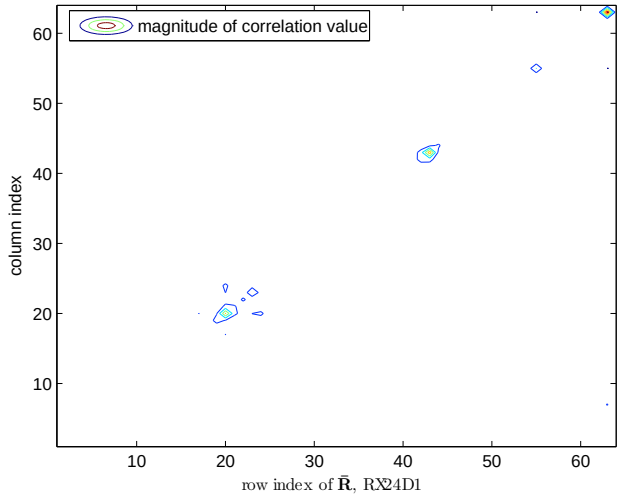

Figure 5: Contour plot of narrowband virtual channel correlation matrix $\bar{\mathbf{R}}$.

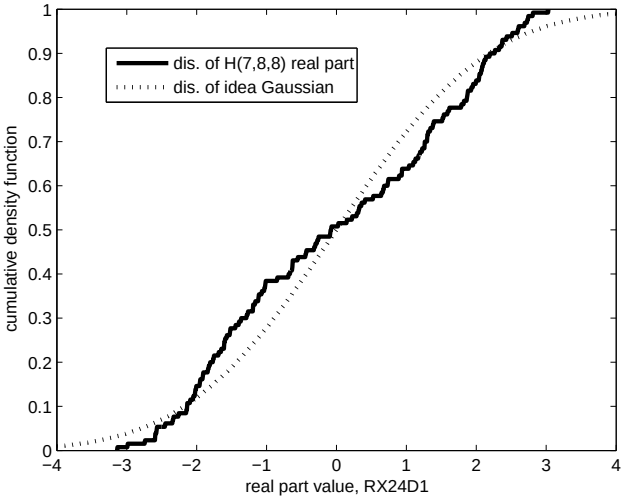

Figure 6: Cumulative distribution function of $H(7,8,7)$ real part.

is chosen to equalize the powers of X and $H(7,8,7)$. Furthermore, the experimental results indicate that $H(q,p)$ is more Gaussian than the corresponding $H(q,p,l)$, since $H(q,p)$ is contributed by more paths due to the lack of resolvability in the delay domain. As an application, the non-Gaussian distribution can be exploited to generate more accurate error probability formulae for antenna diversity systems, since $\{H(q,p,l)\}$ represent the amplitudes of resolvable paths in the angle-delay domain, whose statistics determine the diversity performance.

4.4 Space-Frequency Correlation

The space-frequency correlation matrix is defined as $\mathbf{R}_{SF} = E[\boldsymbol{h}\boldsymbol{h}^H]$ with $\boldsymbol{h}$ comprising the $N_R N_T N_F$ actual channel coefficients in $\{\mathbf{H}_c(f_m)\}_{m=1}^{N_F}$. The experimental results show that $\mathbf{R}_{SF}$ is fundamentally determined by $\{M(q,p,l)\}$, which represents the 3D power spectrum in the virtual angle-delay domain. Specifically, we define the estimated correlation matrix $\widehat{\mathbf{R}}_{SF}$ by replacing each entry in $\mathbf{R}_{SF}$ with the value approximated by $\{M(q,p,l)\}$ via (22). The normalized mean square error $\| \mathbf{R}_{SF} - \widehat{\mathbf{R}}_{SF} \|_F^2 \; / \; \| \mathbf{R}_{SF} \|_F^2$ measured at different sites is

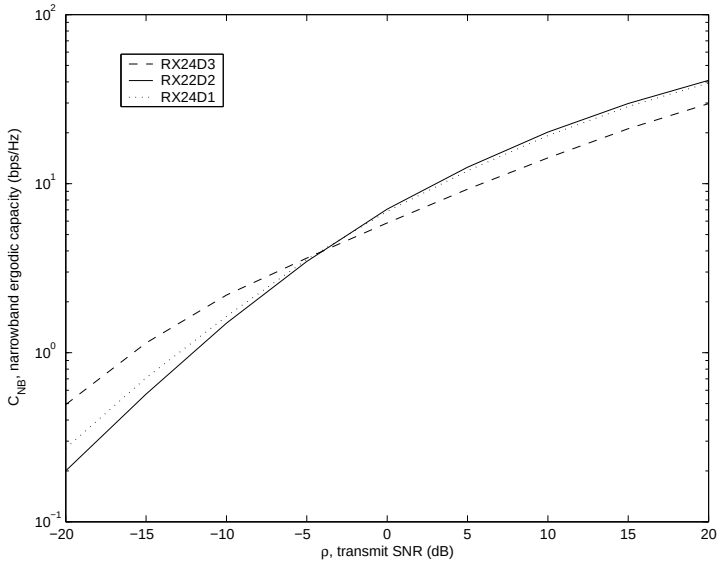

Figure 7: Capacity comparison of 3 typical scattering environments: RX24D3, RX22D2, and RX24D1.

found to be between 0.023 to 0.041, which shows a good match of the two. It means that the space-frequency correlation can be efficiently represented by the non-vanishing $M(q,p,l)$'s, whose number is much smaller[6] than the number of elements in $\mathbf{R}_{SF}$ and that of physical path parameters.

4.5 Capacity of Different Scattering Environments

As introduced earlier, the narrowband virtual channel power matrix $\mathbf{M}$ serves as the 2D angular power spectrum, which is determined by the physical scattering environments. Suppose the total channel power $\sum_q \sum_p M(q,p)$ is fixed, the analysis in Section III-A indicates that at low SNR, the $\mathbf{M}$ maximizing the capacity upper bound has all the non-vanishing entries distributed in one column, while at high SNR, the upper bound is maximized when the entries of $\mathbf{M}$ have equal value. Those insights can explain the capacity behavior under different scattering environments. The narrowband capacity is computed via (25) for 3 typical measurement scenarios: RX24D1, RX24D3, and RX22D2. The $\mathbf{M}$ of RX24D1 has 4 dominant entries, as shown in Fig.4. The $\mathbf{M}$ of RX24D3 has a unique dominant entry $M(3,3)$ corresponding to a spiky angular spectrum. For RX22D2, the entry values of $\mathbf{M}$ have the least variance among the three, which leads to a rather flat spectrum. It can be observed from Fig.7 that at low SNR, the capacity is maximized by RX24D3, whose channel power is mainly concentrated in the 3rd column, while at high SNR, the capacity is maximized by RX22D2, which has the flattest spectrum. For RX24D1, the angular spectrum is smoother than RX24D3 but is more peaky than RX22D2 and, therefore, its capacity is sandwiched by the other two. This result suggests that a sparse $\mathbf{M}$ will favor the capacity at low SNR, while a smooth $\mathbf{M}$ will benefit the capacity at high SNR.

[6]Note that the number of non-vanishing $M(q,p,l)$'s is at most $N_T N_R L$, the number of elements in $\mathbf{R}_{SF}$ is $(N_T N_R N_F)^2$ with N_F much greater than L in general, and the number of physical path parameters is greater than that of non-vanishing $M(q,p,l)$'s, as discussed earlier.

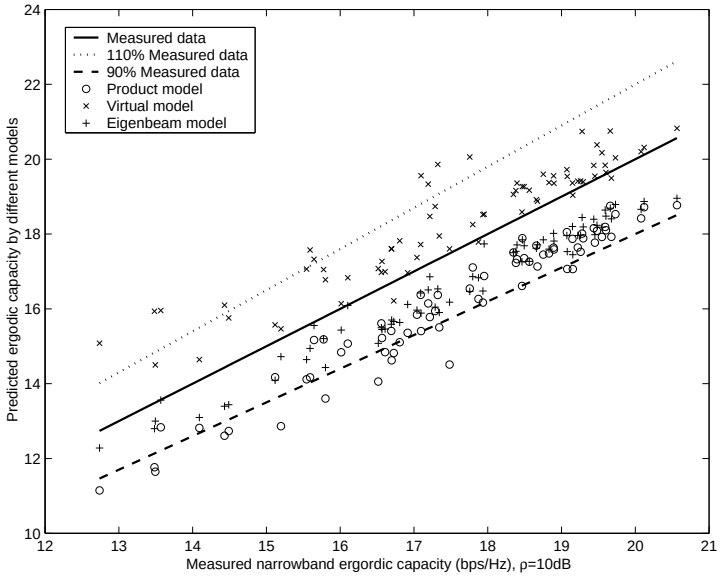

Figure 8: Predicted ergodic capacity vs. measured ergodic capacity for different channel models.

4.6 Capacity Prediction by Different Channel Models

In general, representing the realistic MIMO channels through a simple mathematical model is a challenging task due to the complicated channel statistics. In this subsection, the virtual channel model is compared to other models introduced in Section III-B with the narrowband capacity C_{NB} as the performance index. In Fig.8, C_{NB} predicted by different models is plotted against the measured value for all 72 measurement scenarios. For each model, the synthesized channel realizations are used in (25) to compute C_{NB}. Each data point in the figure corresponds to a specific model and a specific scenario. The solid line[7] represents the C_{NB} computed with the measured data. It can be observed that both the Kronecker and eigenbeam models in (30) and (32) always underestimate C_{NB}, while the virtual model in (29) usually generates a higher prediction. To numerically evaluate the performance, we compute the normalized mean square error for each model which is defined as $\| \boldsymbol{C} - \widehat{\boldsymbol{C}} \|_F^2 \; / \; \| \boldsymbol{C} \|_F^2$, where $\boldsymbol{C}$ and $\widehat{\boldsymbol{C}}$ represent the 72×1 measured and predicted capacity vectors. The mean square error is 0.0035 for both the virtual and eigenbeam models and is 0.0072 for the Kronecker model. Therefore, both the virtual and eigenbeam models in general give better prediction than the Kronecker model.

As for the Kronecker model, the spatial correlation is modeled as the product of the corresponding receive and transmit correlations [4]: $E\big[H_c(i,k)H_c^*(i',k')\big] = E\big[H_c(i,k)H_c^*(i',k)\big]$ $E\big[H(i,k)H^*(i,k')\big]$. According to (24), this implies that each entry of the virtual channel power matrix should have a product form: $M(q,p) = M_R(q)M_T(p)$, and the receive and transmit correlations are determined by the vectors $\boldsymbol{M}_R = [M_R(1), \ldots, M_R(N_R)]^T$ and $\boldsymbol{M}_T = [M_T(1), \ldots, M_T(N_T)]^T$, respectively. The corresponding $\mathbf{M}$ has a separable structure: $\mathbf{M} = \boldsymbol{M}_R \boldsymbol{M}_T^T$. The measured $\mathbf{M}$ indicates that it is usually not the case. For instance, if the $\mathbf{M}$ in Fig.4 has a separable structure, there should have 9 dominant entries at the intersections of the 3 dominant transmit and receive virtual angles. The outer-product structure imposed on $\mathbf{M}$ could account for the relatively large prediction error of the Kronecker model. This point is

[7]The measured capacity points are first plotted against themselves and hence are distributed on a 45° line. They are further connected to be a solid line, which can be better distinguished from the predicted capacity points.

basically consistent with the results in [17][18].

The smaller errors of the virtual and eigenbeam models are due to the modeling of non-separable spectrum. Specifically, $\mathbf{M}$ and $\mathbf{\Omega}$ in (32) are not assumed to be separable. The accuracy of the virtual model is mainly limited by the residual correlation among the virtual channel coefficients due to the non-vanishing side lobes of the Fourier beams. The accuracy of the eigenbeam model is mainly limited by its assumption. To describe it, we express the spatial-domain channel matrix as $\mathbf{H}_c = [\boldsymbol{h}_1, \cdots, \boldsymbol{h}_{N_T}] = [\boldsymbol{g}_1, \cdots, \boldsymbol{g}_{N_R}]^H$ where $\boldsymbol{h}_k$ and $\boldsymbol{g}_i^H$ denote the k-th column and i-th row of $\mathbf{H}_c$, respectively. We further define $\mathbf{U}_R(k,k')$ and $\mathbf{U}_T(i,i')$ as the matrices containing the orthonormal eigenvectors of $E[\boldsymbol{h}_k \boldsymbol{h}_{k'}^H]$ and $E[\boldsymbol{g}_i \boldsymbol{g}_{i'}^H]$ respectively. It has been shown in [24] that the entries of $\mathbf{H}_{\text{eig}}$ in (31) will be uncorrelated if $\mathbf{U}_R(k,k') = \mathbf{U}_R$ and $\mathbf{U}_T(i,i') = \mathbf{U}_T$ regardless of the indices $\{k,k'\}$ and $\{i,i'\}$. To investigate this assumption, we compare $\mathbf{U}_R(k,k')$ with $\mathbf{U}_R$ and define the error as $\| \mathbf{U}_R(k,k') - \mathbf{U}_R \|_F^2 \,/\, \| \mathbf{U}_R \|_F^2$ averaged over all (k,k'). The error is found to be 1.71 and the error corresponding to $\mathbf{U}_T$ is 1.91. Therefore, the modeling error might be due to the mismatch of the eigenbasis, which impairs the assumption of uncorrelated $\mathbf{H}_{\text{eig}}$ entries.

Compared to the eigenbeam model, the virtual model has low modeling complexity. To characterize the channel statistics, the eigenbeam model needs $\mathbf{\Omega}$, $\mathbf{U}_R$, and $\mathbf{U}_T$, while the virtual model only needs $\mathbf{M}$ due to the use of fixed Fourier basis. This will favor the design of wireless systems, which require the feedback of channel statistics, since the feedback cost will be reduced by only transmitting $\mathbf{M}$.

5 Conclusions

This work presents an experimental study of MIMO channel statistics and capacity via the virtual channel representation, which describes the channel via the virtual paths at fixed virtual angles and delays. Detailed results are summarized below.

- **Angle-delay dependencies**: The conditional angular power spectrum represented by $\mathbf{M}(l)$ varies with the virtual delay index l, and the dominant entries in each $\mathbf{M}(l)$ have a smaller angular spread than those in the narrowband angular spectrum $\mathbf{M}$. The smaller angular spread implies a sparse distribution of essential degrees of freedom in the virtual angle-delay domain, which can be exploited for an efficient low-rank approximation of the actual channel matrix.
- **Statistics of virtual channel coefficients**: Both the narrowband and wideband virtual channel coefficients are approximately uncorrelated, since each virtual coefficient is contributed by a distinct set of physical paths according to (17) and (19). The virtual coefficients may have non-Gaussian marginal statistics due to the contribution of a finite number of physical paths.
- **Space-frequency correlation**: The actual channel coefficients in $\{\mathbf{H}_c(f_m)\}_{m=1}^{N_F}$ form a 3D space-frequency stationary process whose correlation can be efficiently represented by $\{\mathbf{M}(l)\}_{l=0}^{L}$, which serve as a 3D power spectrum in the virtual angle-delay domain.
- **Capacity of different scattering environments**: In the narrowband case, the scattering environment whose $\mathbf{M}$ has all the non-vanishing entries distributed in one column will favor the capacity at low SNR, while the environment with a smooth $\mathbf{M}$ will benefit the capacity at high SNR.
- **Capacity prediction by different channel models**: Both the virtual and eigenbeam models achieve good capacity-prediction accuracy due to the modeling of non-separable

spectrum, while the Kronecker model imposes an outer-product structure on $\mathbf{M}$ and hence results in a larger prediction error.

References

[1] I.E. Telatar, "Capacity of multi-antenna gaussian channels," Tech. Rep., AT&T Bell Labs., 1995.

[2] G.J. Foschini and M.J. Gans, "On the limits of wireless communications in a fading environment when using multiple antennas," Wireless Personal Communications, vol. 6, no. 3, pp. 311-335, Mar. 1998.

[3] D. Shiu, G.J. Foschini, M.J. Gans, and J.M. Kahn, "Fading correlation and its effect on the capacity of multielement antenna systems," IEEE Trans. Commun., vol. 48, pp. 502-513, Mar. 2000.

[4] C.N. Chua, J.M. Kahn, and D. Tse, "Capacity of multi-antenna array systems in indoor wireless environment," in Proc. of IEEE Global Telecommunications Conference, pp. 1894-1899, 1998.

[5] C-N Chuah, D.N. Tse, J.M. Kahn, and R.A. Valanzuela, "Capacity scaling in MIMO wireless systems under correlated fading," IEEE Trans. Inform. Theory, vol. 48, no. 3, pp. 637-650, Mar. 2002.

[6] G. German, Q. Spencer, L. Swindlehurst, and R. Valenzuela, "Wireless indoor channle modeling: statistical agreement of ray tracing simulations and channel sounding measurement," in Proc. IEEE ICASSP, pp. 2501-2504, 2001.

[7] A.F. Molisch, M. Steinbauer, M. Toeltsch, E. Bonek, and R.S. Thoma, "Capacity of MIMO systems based on measured wireless channels," IEEE J. Selec. Areas. Commun., vol. 20, no. 3, pp. 561-569, Apr. 2002.

[8] S.J. Fortune, D.H. Gay, B.W. Kernighan, O. Landron, R.A. Valenzuela, and M.H. Wright, "WiSE design of indoor wireless systems: practical computation and optimization," IEEE Comput. Sci. Eng., vol. 2, pp. 58-68, Mar. 1995.

[9] A.J. Paulraj and C.B. Papadias, "Space-time processing for wireless communications," IEEE Signal Processing Magazine, pp. 49-83, Nov. 1997.

[10] J. Fuhl, A.F. Molisch, and E. Bonek, "Unified channel model for mobile radio systems with smart antennas," IEE Proc. Radar, Sonar Navig., vol. 145, no. 1, pp. 32-41, Feb. 1998.

[11] A.M. Sayeed, "Deconstructing multi-antenna fading channels," IEEE Trans. Signal Processing, vol. 50, no. 10, pp. 2563-2579, Oct. 2002.

[12] A.M. Sayeed and V. Veeravalli, "The essential degrees of freedom in space-time fading channels," in Proc. IEEE PIMRC, Lisbon, Portugal, pp. 1512-1516, Sep. 2002.

[13] V. Veeravalli, Y. Liang, and A. Sayeed, "Correlated MIMO wireless channels: capacity, optimal signaling and asymptotics," to appear in IEEE Transactions on Information Theory, 2005.

[14] K. Liu, V. Raghavanand, and A.M. Sayeed, "Capacity scaling and spectral efficiency in wideband correlated MIMO channels," IEEE Trans. Inform. Theory, vol. 49, no. 10, pp. 2504 - 2526, Oct. 2003.

[15] M. Steinbauer, A.F. Molisch, and E. Bonek, "The double directional radio channel," IEEE Antenna and Propagation Magazine, vol. 43, no. 4, pp. 51-63, Aug. 2001.

[16] M. Herdin, H. Ozcelik, H. Hofstetter, and E. Bonek, "Linking reduction in measured MIMO capacity with dominant-wave propagation," in Proc. IEEE ICT, pp. 1526-1530, Feb. 2003.

[17] H. Ozcelik, M. Herdin, R. Prestros, and E. Bonek, "How MIMO capacity is linked with multipath distribution," in Proc. International Conference on Electromagnetics in Advanced Applications, Torino, Italy, pp. 775-778, Sep. 2003.

[18] H. Ozcelik, M. Herdin, W. Weichselberger, J. Wallace, and E. Bonek, "Deficiencies of 'Kronecker' MIMO radio channel model," Electronics Letters, pp. 1209-1210, Aug. 2003.

[19] K. Liu and A.M. Sayeed, "Space-Time D-Block Codes via the Virtual MIMO Channel Representation," IEEE Trans. on Wireless Commun., vol. 3, pp. 982-991, May 2004.

[20] J. Kotecha and A.M. Sayeed, ”Optimal estimation of correlated MIMO channels,” IEEE Trans. on Signal Processing, vol. 52, no. 2, pp. 546-557, Feb. 2004.

[21] Z. Hong, K. Liu, R. Heath, and A.M. Sayeed, ”Spatial multiplexing in correlated fading via the virtual channel representation,” IEEE JSAC, vol. 21, no. 5, pp. 856-866, June 2003.

[22] K. Yu, M. Bengtsson, B. Ottersten, P. Karlsson, and M. Beach, ”Second order statistics of NLOS indoor MIMO channels based on 5.2 Ghz measurements,” in Proc. of IEEE Global Telecommunications Conference, vol. 1, pp. 156-160, 2001.

[23] W. Weichselberger, M. Herdin, H. Ozcelik, and E. Bonek, ”A stochastic MIMO channel model with joint correlation of both link ends,” IEEE Trans. on Wireless Commun., vol. 5, pp. 90-100, Jan. 2006.

[24] W. Weichselberger, H. Ozcelik, M. Herdin, and E. Bonek, ”A novel stochastic MIMO channel model and its physical interpretation,” in Proc. International Symposium on Wireless Personal Multimedia Communications, Yokosuka, Japan, October, 2003.

[25] T.M. Cover and J.A. Thomas, Elements of Information Theory. Wiley, 1991.

[26] J. Kotecha and A.M. Sayeed, ”Canonical statistical models for correlated MIMO fading channels and capacity analysis,” submitted to IEEE Trans. on Wireless Communications.

[27] A. M. Sayeed, V. Raghavan, and J. Kotecha, ”Capacity of Space-time Wireless Channels: A Physical Perspective”, in Proc. IEEE Information Theory Workshop, pp. 434-439, Oct. 2004.